THE JOURNAL OF BIOLOGICAL CHEMISTRY VOL. 291, NO. 32, pp. 16494–16507, August 5, 2016

Solution Structures of Complement C2 and Its C4 Complexes Propose Pathway-specific Mechanisms for Control and Activation of the Complement Proconvertases*[S]

Received for publication, February 17, 2016, and in revised form, May 27, 2016 Published, JBC Papers in Press, June 1, 2016, DOI 10.1074/jbc.M116.722017

Sofia Mortensen[1], **Jan K. Jensen, and Gregers R. Andersen**[2]

From the Department of Molecular Biology and Genetics, Aarhus University, Gustav Wieds Vej 10C, DK-800 Aarhus, Denmark

The lectin (LP) and classical (CP) pathways are two of the three main activation cascades of the complement system. These pathways start with recognition of different pathogen- or danger-associated molecular patterns and include identical steps of proteolytic activation of complement component C4, formation of the C3 proconvertase C4b2, followed by cleavage of complement component C2 within C4b2 resulting in the C3 convertase C4b2a. Here, we describe the solution structures of the two central complexes of the pathways, C3 proconvertase and C3 convertase, as well as the unbound zymogen C2 obtained by small angle x-ray scattering analysis. We analyzed both native and enzymatically deglycosylated C4b2 and C2 and showed that the resulting structural models were independent of the glycans. The small angle x-ray scattering-derived models suggest a different activation mode for the CP/LP C3 proconvertase as compared with that established for the alternative pathway proconvertase C3bB. This is likely due to the rather different structural and functional properties of the proteases activating the proconvertases. The solution structure of a stabilized form of the active CP/LP C3 convertase C4b2a is strikingly similar to the crystal structure of the alternative pathway C3 convertase C3bBb, which is in accordance with their identical functions in cleaving the complement proteins C3 and C5.

The human complement system performs a broad range of roles, including defense against invading pathogens, modulation of adaptive immune system responses, and maintenance of the body's homeostasis (1, 2). The lectin (LP)[3] and classical (CP) pathways are two of the main activation cascades of complement. They are triggered when pattern recognition molecules, C1q in the CP and the collectins/ficolins in the LP, bind to molecular patterns associated with pathogens or altered self (3, 4). Upon binding, the proteases associated with the pattern recognition molecules become active, C1r and C1s in the CP and MBL-associated serine proteases (MASP)-1 and MASP-2 in the LP. C1s and MASP-2 subsequently cleave complement component C4, generating C4b (Fig. 1*A*) (5). C4b adopts a conformation very different from that of C4 (6) and binds the zymogen C2 in a Mg^{2+}-dependent manner (7). Together they form the CP/LP C3 proconvertase complex, C4b2. Within this complex, C2 can be cleaved by C1s, MASP-1, and MASP-2 into two fragments as follows: the large C2a, comprising a von Willebrand factor (vWf) domain and a serine protease (SP) domain, and the smaller C2b consisting of three complement control protein (CCP) domains (7–9). C2b dissociates (10) whereas C2a stays bound to C4b, forming the CP/LP C3 convertase C4b2a (11). Two areas in C2 are involved in binding to C4b in the proconvertase. One is located on the CCP1-3 domains (12), and the second is the metal ion-dependent adhesion site (MIDAS) of the vWf domain that coordinates a Mg^{2+} ion under physiological conditions (13). Within the C3 convertase, the MIDAS interaction is essential for the binding of C2a to C4b. C4b2a is an unstable complex with a half-life of 5 min at 37 °C (14); its dissociation is presumably accompanied by a change in C2a conformation, which prevents reassociation (8). The cleavage of complement component C3 by the CP/LP C3 convertase triggers the downstream effector events such as signal transduction by the anaphylatoxins, stimulation of phagocytosis, and assembly of the cell membrane attack complex.

Complement C3 and factor B (FB) are the key players in the third main complement activation cascade, the alternative pathway (AP), and are paralogues of C4 and C2, respectively. The formation of the AP C3 proconvertase and convertase include steps equivalent to those leading to assembly of the CP/LP equivalents. FB binds C3b to form the AP proconvertase C3bB. Subsequently, FB is cleaved by factor D (FD) resulting in the generation of the AP C3 convertase C3bBb. As C4b2a, the AP convertase quickly undergoes irreversible dissociation (15, 16). Comprehensive structural information concerning the interactions and conformational changes taking place during formation of the AP complexes was obtained from crystal structures and electron microscopy studies of C3b, FB, Bb, C3bB, and C3bB in complex with FD, cobra venom factor (CVF, a paralogue of C3b) in complex with FB, and C3bBb in complex with inhibitor SCIN. According to these structural studies and available biochemical data, C3bB and C3bBb are formed as follows. Unbound FB adopts the so-called closed conformation in which the scissile bond Arg-259–Lys-260 is protected from FD

* The authors declare that they have no conflicts of interest with the contents of this article.

[S] This article contains supplemental Fig. 1.

[1] Recipient of a Boehringer-Ingelheim Fonds Ph.D. fellowship.

[2] To whom correspondence should be addressed: Dept. of Molecular Biology and Genetics, Aarhus University, Gustav Wieds Vej 10C, DK-8000 Aarhus, Denmark. Tel.: 45-51446530; E-mail: gra@mbg.au.dk.

[3] The abbreviations used are: LP, lectin pathway; CP, classical pathway; SAXS, small angle x-ray scattering; AP, alternative pathway; SP, serine protease; SPR, surface plasmon resonance; MIDAS, metal ion-dependent adhesion site; vWf, von Willebrand factor; CCP, complement control protein; FD, factor D; FB, factor B; SEC, size exclusion chromatography; RALS, right angle light scattering; RI, refractive index; CVF, cobra venom factor; Endo, endoglycosidase; sm, stabilizing mutation; TE, thioester; RU, response unit; MBP, maltose-binding protein.

cleavage (17). Upon binding of FB to C3b, two sets of contacts are established, one between the CCP1-3 domains of FB and C3b and another between the FB MIDAS and the carboxylate group in the C-terminal C3b residue (18, 19). A slow conformational change then occurs, which includes a dramatic movement of the FB SP domain, resulting in the adoption of the so-called open conformation of FB and its scissile bond becoming susceptible to FD cleavage (18–20). The crystal structures of CVFB and C3bB represent the AP proconvertase before and after this conformational change, respectively (18, 19). Formation of C3bB in the presence of Mg^{2+} ions results in a mixture of the two conformations (21). Substitution of Mg^{2+} by Ni^{2+} shifts the equilibrium to an almost homogeneous population of C3bB in the open state (21). FD binding to C3bB also shifts the equilibrium toward the open conformation (19).

In contrast to the wealth of functional and structural studies of FB and AP proconvertase and convertase, much less is known about the CP/LP proteins. To depict how complement activation proceeds in the CP/LP, we performed SAXS and surface plasmon resonance (SPR) experiments on the proteins from the CP/LP. Our studies suggested differences in the activation of C2/C4b2 and FB/C3bB that may be rationalized by the distinct nature of the proteases activating them. We also describe the first solution structure of the central complex of the CP/LP, the C3 convertase C4b2a, suggesting that its architecture is similar to that of the AP C3 convertase.

Results

Preparation of C4b and C2—To analyze the solution structure of C2, we prepared recombinant C2 by expression in HEK293 cells (Fig. 1*B*). We then generated deglycosylated C2 by treatment with four endoglycosidases to remove as much glycan as possible. Both native and deglycosylated C2 could bind C4b. C2 contains eight Asn-linked glycans (UniProt entry P06681), and assuming a molecular mass of 2 kDa for such a glycan, this adds 16 kDa to the 83 kDa calculated from the protein sequence in agreement with a broad band of C2 with an apparent molecular mass of ~100 kDa in SDS-PAGE (Fig. 1*C*). After deglycosylation, C2 migrated with an apparent molecular mass of ~80–85 kDa, suggesting that the majority of the Asn-linked glycans were removed (Fig. 1*D*). C4b is modified with four Asn-linked glycans (UniProt entry P0C0L4), three in the α'-chain and one in the β-chain. Enzymatic treatment with the four endoglycosidases reduced the apparent molecular mass in SDS-PAGE of both chains in agreement with their glycan content (Fig. 1*D*). In the following SAXS modeling, we assumed for simplicity that both proteins were fully deglycosylated, but removal may not be complete in reality.

C2 SAXS Data Collection and Analysis—Data for glycosylated and deglycosylated C2 samples were recorded at protein concentrations of 10, 5, and 2.5 mg/ml. An analysis of the calculated R_g and $I(0)$ values suggested that C2 oligomers contributed to the scattering at the two highest concentrations, especially for deglycosylated C2. To exclude oligomer contributions and to enable a direct comparison between models derived by rigid body refinement, we used the data collected at 2.5 mg/ml for both forms of C2. The overall structural parameters derived directly from these two datasets are presented in Table 1.

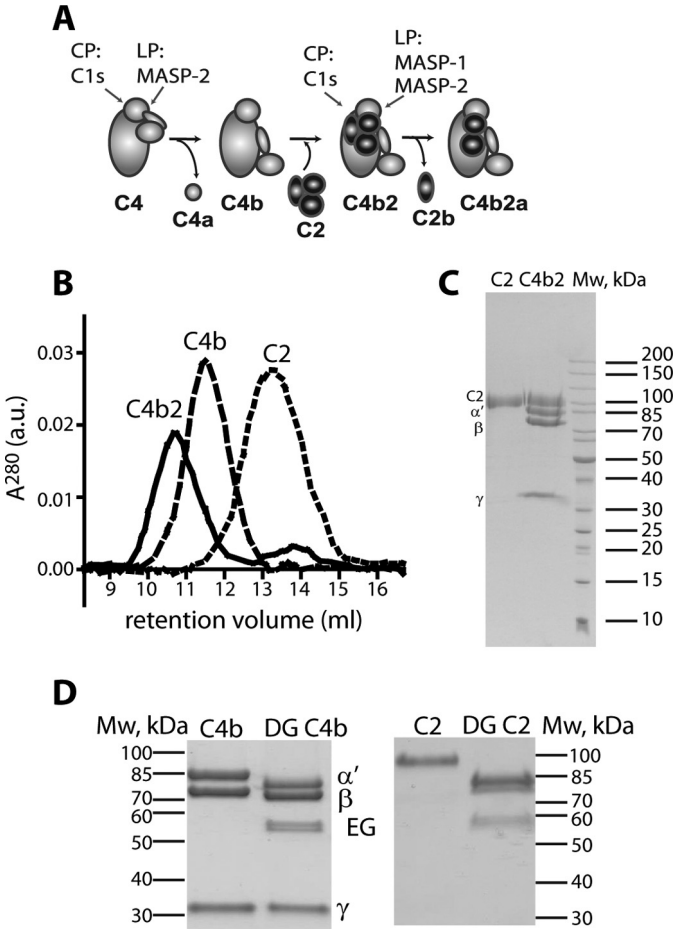

FIGURE 1. **Scheme of the CP and LP pathways of complement and preparation of C2 and C4b2 samples for SAXS experiments.** *A,* events occurring within the CP and LP after pattern recognition and activation of the initiating proteases C1s, MASP-1, and MASP-2. C1s and MASP-2 cleave C4 with generation of C4b. C2 binds C4b, which results in formation of the C3 proconvertase C4b2. C2 within C4b2 is subsequently cleaved by C1s, MASP-1, and MASP-2 with generation of the C3 convertase C4b2a. *B,* size exclusion chromatography of 0.83 nmol of purified C4b (158 μg/450 μl), 1.81 nmol of C2 (180 μg/450 μl), and C4b2 formed by mixing 0.55 nmol of C4b with 0.60 nmol of C2 (105 μg + 60 μg/450 μl). *C,* SDS-PAGE analysis under reducing conditions of the glycosylated C2 (1.7 μg) and C4b2 (4.4 μg) samples used for SAXS data collection. The positions of C2 and the C4b chains α', β, and γ are indicated. *D,* SDS-PAGE analysis of the enzymatic treatment of C4b and C2 with the four endoglycosidases. C2 containing eight Asn-linked glycans shows a significant reduction in molecular mass after treatment. The large shift of the C4b α'-chain band and the smaller shift of the β-chain band are in agreement with the *N*-linked glycan contents of the chains. The bands below 60 kDa marked *EG* in both gels contains the GST- and MBP-tagged endoglycosidases.

Guinier analysis of the datasets showed a good linear fit (R^2 of 0.99) in the low s region ($s{\cdot}R_g$ <1.3) and suggested R_g values around 35 Å (Fig. 2, *A* and *B*, and Table 1). The pair distance distribution functions exhibited tails in the longer distance region proposing that C2 has an elongated shape (Fig. 2*C*). Estimations of the molecular mass of C2 gave values in reasonable agreement with those expected based on the protein sequence and the glycan content (Table 1) and suggested that the enzymatic deglycosylation of C2 was almost complete.

CORAL Modeling of C2—We constructed models of deglycosylated C2 using the crystal structures of the C2 paralogue FB and the structures of the C2b and C2a fragments. We first prepared a model based on the closed conformation of FB known from its unbound state and when bound to CVF (17, 18). The

TABLE 1

Parameters of the C2, C4b2, and C4b2 particles derived by analysis of the SAXS data collected for C2 and C4b2 samples in batch mode and before (frames 1730–1799) and after (frames 1800–1869) the peak of C4b2a elution during the in-line SAXS run

	C2 (2.5 mg/ml)		C4b2 (2.5 mg/ml)		C4b2a (in-line)	
	With glycans	Deglycosylated	With glycans	Deglycosylated	Frames 1730–1799	Frames 1800–1869
Guinier analysis						
Points in the linear range $s \cdot R_g < 1.3$	27–137	15–130	18–82	17–87	5–77	11–79
R_g, Å	34.8 ± 0.16	35.7 ± 0.17	53.7 ± 0.2	51.3 ± 0.19	49.3 ± 0.1	48.3 ± 0.1
M_r based on $I(0)$[a]	97 ± 0.3	79.6 ± 0.2	292 ± 0.7	258 ± 0.6		
Indirect Fourier transform analysis						
R_g, Å	35.8 ± 0.1	36.9 ± 0.16	54.4 ± 0.14	52.5 ± 0.11	50 ± 0.05	49.1 ± 0.05
M_r based on $I(0)$[a]	96.9 ± 0.2	79.9 ± 0.2	292.2 ± 0.5	252.8 ± 0.4		
D_{max}, Å	130	130	190	180	160	155
M_r from SAXS MOW,[b] kDa					237	
M_r from protein sequence, kDa	83	83	263	263	237	
M_r, including glycans, kDa	99		288		258	

[a] Molecular weight (M_r) was determined using forward scattering value $I(0) = 1843$ of the BSA (72 kDa) standard.
[b] As described in Ref. 25.

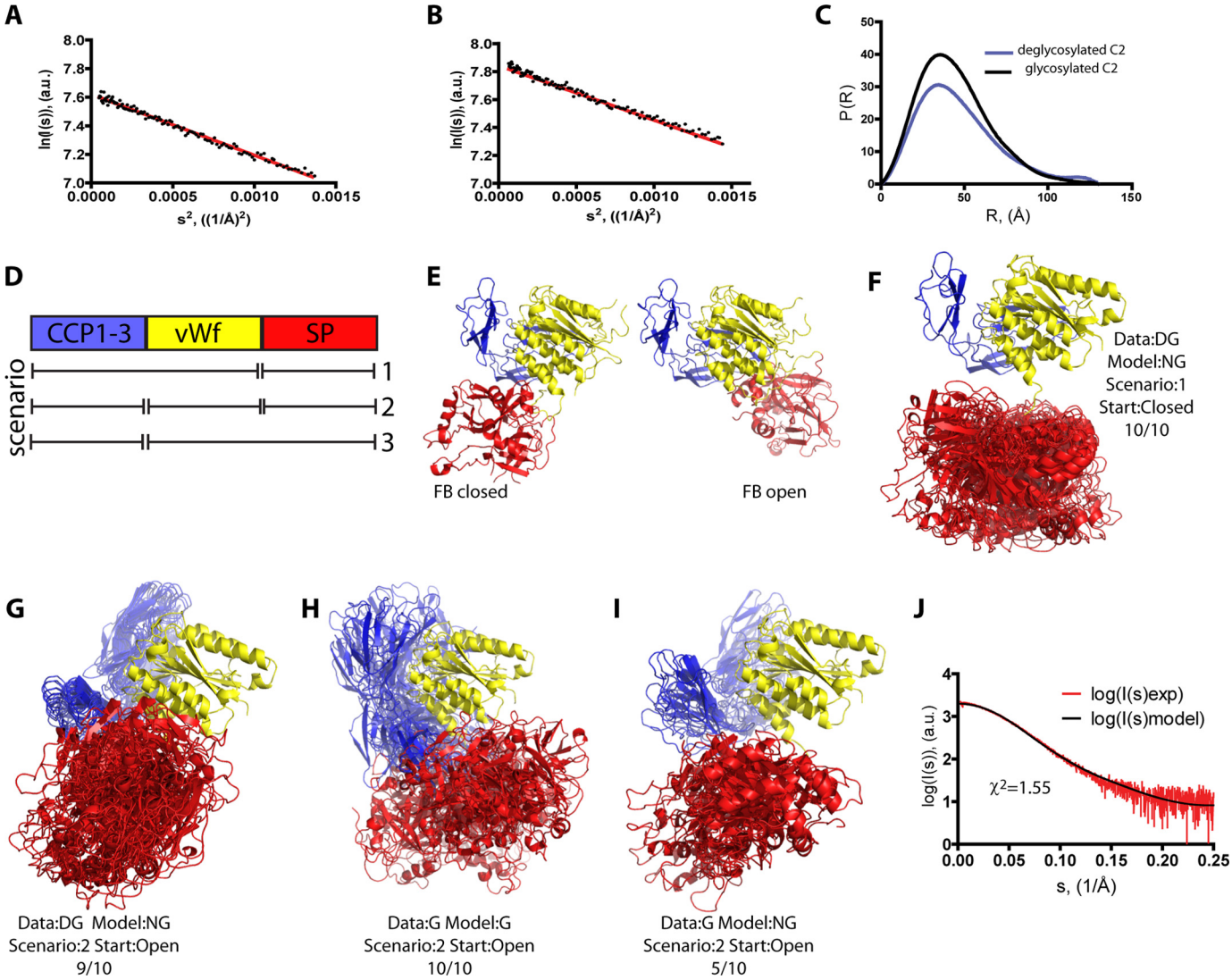

FIGURE 2. **Data processing and rigid body modeling of C2.** *A* and *B*, Guinier plots (ln(*I*(*s*)) as a function of s^2) for deglycosylated (*A*) and glycosylated (*B*) C2 suggest that both samples are not aggregated and devoid of interparticle repulsion. *I*(*s*) is the x-ray scattering intensity, and *s* is the modulus of the scattering vector. *C*, pair distance distribution functions *P*(*r*) exhibiting a maximum inter-atomic distances around 130 Å for both C2 samples. *D*, schematic representation of the rigid bodies in C2 and how they were grouped in the three refinement scenarios. The coloring scheme for the C2 domains is used throughout. *E*, two FB conformations used as templates for the C2 starting models. *F*, C2 models obtained by rigid body CORAL refinement when a non-glycosylated starting model of C2 (model:NG) in the closed conformation (*Start:Closed*) and data from deglycosylated C2 (*Data:DG*) were used and only the SP domain was allowed to move (*scenario 1*). All output models (10/10) from the 10 parallel refinements are shown. *G*, C2 models obtained when starting with a non-glycosylated model of C2 in the open conformation (*Start:Open*) and using three rigid bodies during refinement against data from deglycosylated C2. *H*, as in *G* but after refinements using data obtained with glycosylated C2 (*Data:G*) and model of glycosylated C2 (*Model:G*). *I*, as in *H*, but with a non-glycosylated starting model. *J*, experimental scattering curve (*red*) and the curve calculated with CRYSOL (*black*) from a representative model in *G*.

C2 model was split into three rigid bodies as follows: the CCP1-3, the vWf, and the SP domains (Fig. 2*D*). We tested three different refinement scenarios starting from this model. In scenario 1, the CCP1-3 and the vWf domains were grouped together, whereas the SP domain was free to move relative to the (CCP1-3)–vWf pair. This scenario was based on the observation that the difference between the open and closed conformation of FB is roughly a 90° rotation of the SP domain relative to the vWf and the CCP1-3 domains (Fig. 2*E*). Refinements starting from the closed conformation with scenario 1 resulted in 10 solutions fitting the data with $\chi^2 = 2.26 \pm 0.10$. This may be compared with 10 solutions giving $\chi^2 = 5.40 \pm 0.18$ obtained when only the missing residues in the starting model were modeled by CORAL and the protein domains remained in the starting positions. A visual inspection of the solutions showed that the SP domain had moved significantly from its initial position. All solutions are clustered with the SP domain in a position in-between the closed and the open conformations known for FB (Fig. 2*F*). In scenario 2, we used three rigid bodies, the CCP1-3, the vWf, and the SP domains. The resulting 10 solutions fitted the data with χ^2 of 1.60 ± 0.10. Eight of these solutions were visually similar and had the SP domain moved significantly relative to the vWf domain compared with both the open and the closed FB conformations but not in the same manner as in the scenario 1 solutions (supplemental Fig. S1*A*). In addition, these eight solutions exhibited significant and similar rotations (62–124°) of the CCP1-3 domains relative to the vWf domain, whereas the remaining two solutions had the CCP1-3 domains rotated 51–56° in the opposite direction. We further evaluated scenario 2 with the starting C2 model based on the open FB conformation, which resulted in 10 models giving $\chi^2 = 1.54 \pm 0.05$. Nine of these models clustered very tightly visually (Fig. 2*G*) and were consistent with the cluster of eight solutions, described above, obtained when starting from the closed conformation under scenario 2 (supplemental Fig. S1*A*). In this tight cluster, the CCP1-3 domains were rotated by 62–75° compared with the starting model. We subsequently evaluated whether the movement of the CCP1-3 relative to a single rigid body encompassing both the vWf and the SP domains could explain the data when the refinement started from the open conformation (scenario 3). This resulted in solutions with $\chi^2 = 2.15 \pm 0.21$; 8 of 10 solutions had the CCP1-3 domains rotated (84–121°) in the same manner as observed for scenario 2 (supplemental Fig. S1*B*). Hence, to obtain the best fit to the data, both the SP and the CCP1-3 domains had to be released from the vWf domain as it was in scenario 2. Overall, the rigid body refinement suggested that in deglycosylated C2 the locations of both the CCP1-3 and SP domains relative to the vWf domain are significantly different compared with both the closed and the open conformations of FB.

To analyze the data collected from glycosylated C2, we used a glycan-containing C2 model starting in the open conformation under scenario 2 (11 rigid bodies: CCP1-3, vWf, SP, and eight individual glycans) and scenario 3 (10 rigid bodies: CCP1-3, the vWf and the SP domain grouped, and eight individual glycans). Not surprisingly, the combination of a large number of rigid bodies and the substantial fraction that the glycans constitute of the total mass of C2 allowed CORAL to fit the data quite well with χ^2 values of 1.18 ± 0.03 and 1.19 ± 0.02 for refinement under scenarios 2 and 3, respectively. For scenario 2, 5 out of 10 solutions have some resemblance to those from the equivalent scenario with the data from deglycosylated C2. However, overall there is much less consistency in the resulting conformations, and the location of the SP domain is closer to the starting conformation (Fig. 2*H*). For scenario 3, the output models likewise had their CCP1-3 domains rotated compared with the starting conformation, but there is little consistency between the solutions. In summary, the introduction of the eight glycans as individual rigid bodies made it difficult to evaluate the resulting set of solutions and to distinguish between scenarios that are clearly non-equivalent as judged from their fits to the experimental data from deglycosylated C2.

Hence, unless the overall conformations of glycosylated and deglycosylated C2 are very different, it appeared that the eight glycan rigid bodies prevent CORAL from fitting the three protein rigid bodies into the global minimum. To explore whether the solution structures of glycosylated and deglycosylated C2 differ, we refined the non-glycosylated C2 model in the open conformation against the data from glycosylated C2 under scenario 2. The resulting 10 models fitted the data with $\chi^2 = 2.52 \pm 0.55$, reflecting that the fit to the data is imperfect. Additionally, the resulting models were more diverse than when refined against the deglycosylated C2 data (Fig. 2*I*). However, five of these models were tightly clustered and quite similar to the 9-model cluster obtained for the deglycosylated C2 data (Fig. 2, *I* and *G*) arguing against that deglycosylation leads to a dramatic change in the solution conformation of C2. In conclusion, the most consistent description of the solution conformation structure of C2 is that based on the SAXS data collected from the deglycosylated C2 sample. Both glycosylated and deglycosylated C2 appear to adopt a similar novel conformation as compared with the two well established conformations of FB. The refinement scenario presented in Fig. 2*G* provides the best description of the solution structure of C2. The SAXS curve calculated from a representative member of this cluster showed an excellent agreement with the experimental data (Fig. 2*J*).

SAXS Data Analysis and Modeling of C4b2—As for C2, we collected data from both glycosylated and deglycosylated C4b2 proconvertase. We subsequently selected the data from both samples at 2.5 mg/ml to avoid contributions from oligomers and to allow a direct comparison of the resulting models. The Guinier plots for both datasets had good linear fits in the low *s* region (Fig. 3, *A* and *B*) and gave R_g values of 54 and 51 Å for glycosylated and deglycosylated C4b2, respectively. A tail in the $P(r)$ function calculated by GNOM suggested that both forms of C4b2 are elongated. The estimates of the molecular mass for glycosylated C4b2 based on the $I(0)$ corresponded well to the molecular mass calculated based on the protein sequence and the glycan content. As also observed in the SDS-PAGE analysis (Fig. 1*D*), the molecular mass estimate for deglycosylated C4b2 was 39 kDa lower than for glycosylated C4b2 in agreement with removal of up to 12 Asn-linked glycans upon endoglycosidase treatment (Table 1).

To define the rigid bodies within C4b2 for CORAL refinement, we combined the crystal structure of C4b with our homology models of C2. The intermolecular interaction between

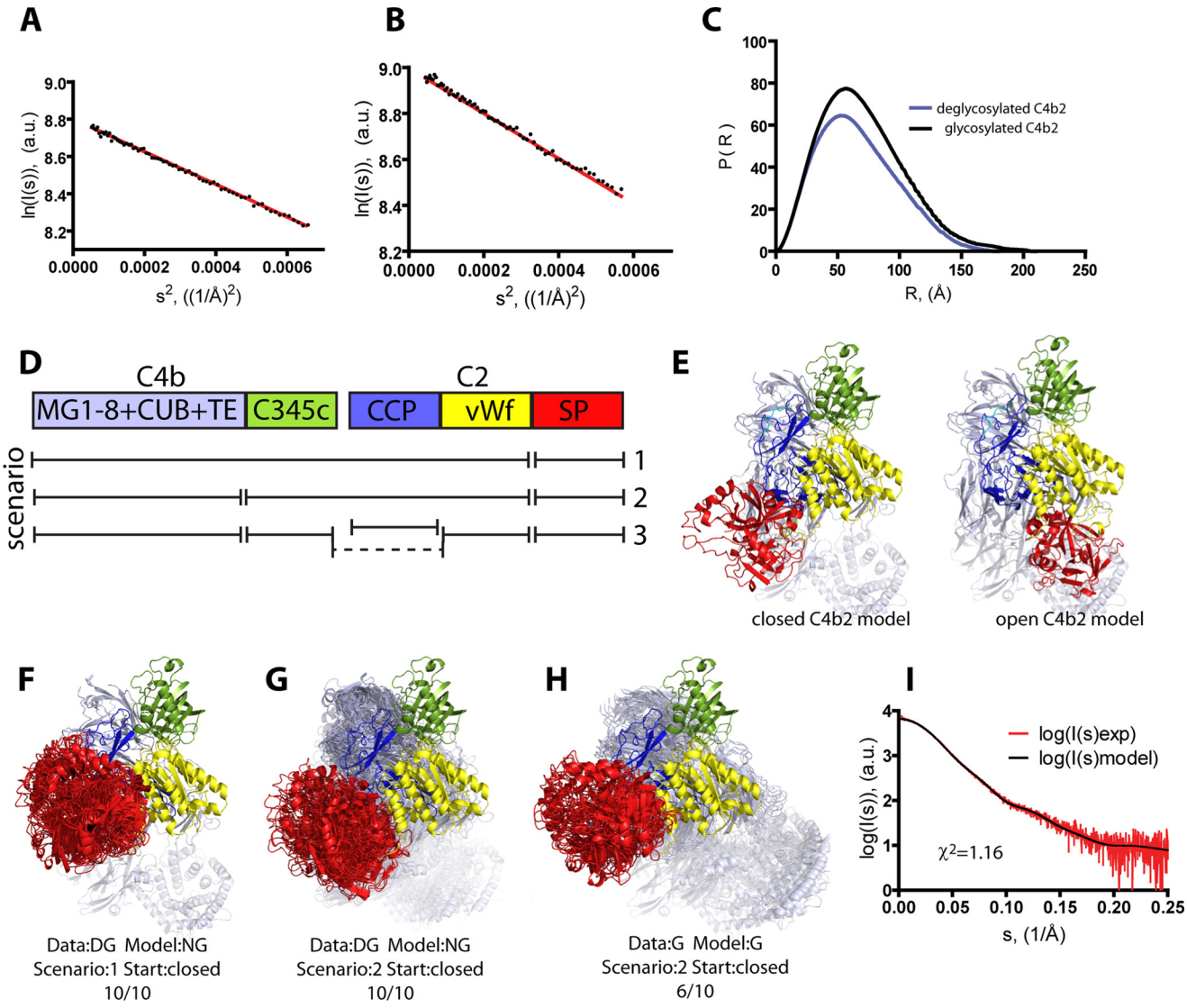

FIGURE 3. **Data processing and modeling of C4b2.** *A* and *B*, linear Guinier plots for deglycosylated (*A*) and glycosylated (*B*) samples suggest that both are non-aggregated and do not suffer from interparticle repulsion. *C*, pair distance distribution functions with maximum inter-atomic distance of 175 and 185 Å for deglycosylated and glycosylated C4b2, respectively. *D*, schematic representation of the rigid bodies defined in the C4b2 complex and how they were grouped in three different modeling scenarios. The colors of the rigid bodies within C4b2 presented in this panel are used also in the following panels presenting molecular models. The *dashed line* in *scenario 3* represents that the C345c and the vWf domains formed a single rigid body. *E*, two starting models of the C4b2 complex based on the CVFB complex (*closed*) and the C3bBD complex (*open*). *F*, models of C4b2 obtained by CORAL refinement using the data from deglycosylated C4b2 and the non-glycosylated C4b2 model starting in the closed conformation and allowing only the C2 SP domain to move. *G*, as in *F* but after refinement under scenario 2. *H*, as in *G* but after a model containing 12 glycans was refined against data from glycosylated C4b2. *I*, experimental scattering curve (*red*) and the curve calculated with CRYSOL (*black*) from a representative model in *G*.

the C3b C345c and FB vWf domains is highly conserved in the structures of C3bB, CVFB, and C3bBb (16, 18, 19). We therefore assumed that C4b and C2 would interact in the same manner and always grouped the C4b C345c domain and the C2 vWf domain into one rigid body. We then tested whether the C4b thioester-containing (TE) domain should be restrained to the MG1 domain as done previously for the SAXS modeling of C4b (6). No significant movement of the TE domain away from the MG core of C4b was observed during CORAL test runs. Therefore, all the C4b domains besides C345c, including the TE and CUB (complement C1r/C1s, Uegf, Bmp1) domains, were grouped into a single rigid body in the arrangement present in the crystal structure of C4b. The third rigid body comprised the CCP1-3 domains of C2b and the fourth the C2 SP domain. We tested three schemes for grouping the four rigid bodies defined above (Fig. 3*D*). In scenario 1, the C2 SP domain was one rigid body, whereas C4b, the C2 vWf, and CCP1-3 domains were grouped together in a second rigid body. In scenario 2, the C2 SP domain also formed one rigid body; a second was formed by grouping the C2 vWf and CCP1-3 domains with the C345c domain from C4b, and the remaining parts of C4b formed a third rigid body. Scenario 3 was identical to scenario 2 except that the CCP1-3 domains here formed a rigid body independent of the C2 vWf and the C4b C345c domains. Starting from our model of non-glycosylated C4b2 in the closed CVFB-like conformation (Fig. 3*E*), refinement under all three scenarios against data collected from deglycosylated C4b2 resulted in tightly clustered models in which the SP domain had rotated to some degree compared with the starting model. But the resulting models still closely resembled the starting closed conforma-

tion. After refinement according to scenario 1, the resulting models (Fig. 3*F*) gave fits to the data with $\chi^2 = 1.48 \pm 0.08$, which was a major improvement compared with the control runs with only refinement of missing regions fitting the data with $\chi^2 = 2.62 \pm 0.14$. An even better fit to the experimental data was obtained in scenario 2 ($\chi^2 = 1.15 \pm 0.04$), and the release of the CCP1-3 domains in scenario 3 only led to minor improvement of the fit ($\chi^2 = 1.07 \pm 0.07$). In both scenarios 2 (Fig. 3*G*) and 3, the C4b C345c domain had also turned relative to the C4b MG7 domain to which it is linked with a disulfide compared with the starting model. A similar rotation was also observed for the C4b solution structure (6). In scenario 3, the CCP1-3 domains had rotated in a variable manner relative to the C2 vWf domain, but they were always located between the C2 vWf domain and the C4b MG6-MG7 domains. The small drop in χ^2 for these models compared with scenario 2 questioned the significance of the CCP1-3 rotations. Similar results were obtained when starting from the open C3bB-like conformation of C2 within C4b2 (Fig. 3*E*). Refinements under both scenario 1 ($\chi^2 = 1.44 \pm 0.15$, see supplemental Fig. S1*C*) and scenario 2 ($\chi^2 = 1.52 \pm 0.21$, see supplemental Fig. S1*D*) starting from the open C4b2 conformation gave models with C2 resembling the closed conformation of FB.

Next, we performed rigid body refinement of the *in silico* glycosylated model of C4b2 in the closed conformation against the data collected from the glycosylated C4b2 complex. In scenario 1 (two protein rigid bodies and 12 glycan rigid bodies), the resulting 10 models (supplemental Fig. S1*E*) fitted the data with $\chi^2 = 1.25 \pm 0.24$ and were all very similar to the models from the equivalent refinement against the data from deglycosylated C4b2. In scenario 2 (three protein rigid bodies and 12 glycans), the 10 output models gave fits with $\chi^2 = 1.17 \pm 0.2$ (Fig. 3*H*). Six of these were again similar to their deglycosylated equivalent, whereas four were closer to the starting model. Refinement under scenario 1 starting from the open conformation also resulted in models similar to those obtained with the closed starting conformation (supplemental Fig. S1*F*). Refinement under scenario 2 starting from an open conformation yielded a structurally much more diverse ensemble of output models (supplemental Fig. S1*G*) as compared with the models obtained from a closed starting model (Fig. 3*H*).

In summary, SAXS rigid body analysis suggested that within both glycosylated and deglycosylated C4b2, the zymogen C2 adopts a conformation resembling the closed state of FB, whereas the C4b subunit has undergone minor adjustments compared with the crystal structure of isolated C4b (6). The position of the SP domain in C4b2 suggested by our SAXS models is rather similar to that of FB in CVFB with the SP domain having no contacts with C4b. The refinement scenario presented in Fig. 3*G* procures reliable models for the solution structure of the proconvertase C4b2. The SAXS curve calculated from a representative model from this scenario exhibited a very satisfying fit to the experimental data (Fig. 3*I*).

Stabilization of C4b2a and SPR Experiments on C4b2 and C4b2a—Structural and functional studies of the C4b2a complex have been challenging due to high instability of the complex. To stabilize the complex, we introduced two mutations, C261A and Q263K, in the MIDAS motif of C2. These mutations were previously reported to prolong activity and half-life of C4b2a in hemolytic assays (13). In the structure of C2a (22), Cys-261 is buried, and its mutation potentially influences the properties of Ser-262. In contrast, Gln-263 is surface-exposed, and introduction of a lysine could lead to additional electrostatic/polar interactions with C4b or C2a residues, altering the backbone properties of Ser-262 and Ser-264, both coordinating the Mg^{2+} ion with their side chain. Noteworthy, mutation of the FB Asp-279 (equivalent of C2 Gln-263) to glycine also confers enhanced stability to the AP convertase (23). Another known means to stabilize the convertase complex is to substitute the physiological Mg^{2+} ion in the MIDAS with Ni^{2+}. Significantly lower concentrations of Ni^{2+} compared with Mg^{2+} were needed to support convertase assembly suggesting that Ni^{2+} binds more tightly to both the AP and the CP/LP C3 convertases (15).

We assessed the impacts of the mutations as well as the metal ion chelation by the MIDAS on stability of both C4b2 and C4b2a by surface plasmon resonance measurements. We captured C4b on a streptavidin SPR sensor chip via a site-specific biotin moiety in a manner that mimics C4b attachment to an activating surface (24). The use of the almost irreversible streptavidin/biotin interaction resulted in a stable C4b-immobilized sensor chip surface with no observable dissociation throughout our experiments. Use of the site-specific capture of C4b allowed us to accurately assign RU changes to mass changes when injecting C2 and following the dissociation of C2, C2b, and C2a. We injected either wild type (C2 WT) or C2 with the two stabilizing mutations (C2 sm) in either Mg^{2+}- or Ni^{2+}-containing buffers onto the immobilized C4b (Fig. 4*A*). The half-lives of dissociation ($t_{½}$) of the formed C4b2 and C4b2a were measured under a variety of conditions (Table 2). All of the formed proconvertase complexes could be disrupted by injection of 5 mM EDTA (Fig. 4*B*, *black curve*) or 1 M NaCl, compatible with electrostatic interaction as an important component of the C4b-C2 interface. C4b2 formed using C2 sm was 1.7 times more stable than the complex formed with C2 WT, and the complex formed in the presence of Ni^{2+} was 1.8 times more stable than that formed in the presence of Mg^{2+} (Fig. 4*D* and Table 2). Formation of C4b2 using C2 sm and Ni^{2+}-containing buffer resulted in a complex being 2.5 times more stable (Fig. 4*D* and Table 2). To follow dissociation of the convertase C4b2a, we cleaved the proconvertase assembled on the sensor chip surface by injecting C1s (Fig. 4*A*). Injection of C1s caused a two-state dissociation. Based on the molecular mass of C2a and C2b and the loss of SPR signal, we assigned the initial very fast dissociation to C2b and the following slow dissociation to C2a (Fig. 4*A*). Importantly, the slow dissociation phase was at least five times slower than C2 dissociation under the same conditions excluding that the slow phase was due to dissociation of uncleaved C2. This was further confirmed by injection of C1s inhibited by PMSF onto preassembled C4b2 (Fig. 4*C*). In this experiment, no fast dissociation phase was observed showing that active C1s was required to elicit the two-phase dissociation behavior. Once formed, C4b2a could not be disrupted by addition of EDTA or high salt suggesting that the MIDAS has somewhat different conformations in C4b2 and C4b2a and is inaccessible for solvent in C4b2a (Fig. 4*B*, *red curve*). These

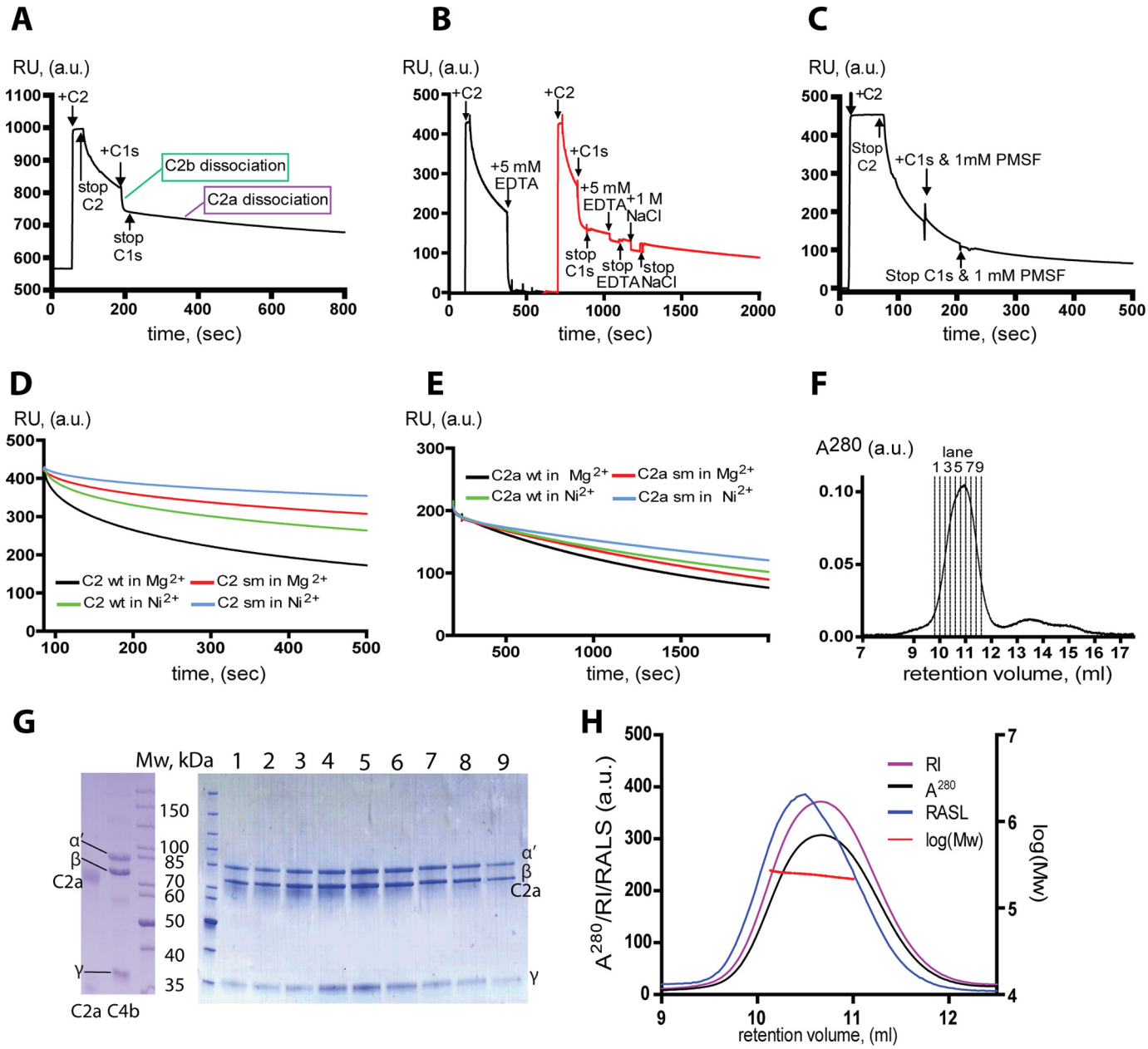

FIGURE 4. **Stabilization and preparation of C4b2a.** *A,* formation of C4b2 and C4b2a on the surface of an SPR sensorchip. Around 600 pg/mm^2 biotinylated C4b (~189 kDa) was captured on a sensorchip, and then C2 (~99 kDa) was injected (*+C2*) resulting in the formation of C4b2. C1s was subsequently injected (*+C1s*), leading to the fast dissociation of C2b (~28 kDa) and the slow dissociation of C2a (~71 kDa). The ends of the C2 and C1s injections are labeled as "*stop C2*" and "*stop C1s*." The flow rate was 30 μl/min. The sensorgram was obtained by subtraction of the RU signal of the reference flow cell without immobilized C4b from the RU signal of the flow cell with immobilized C4b, whereas the sensorgrams in *B–E* were subtracted from the nearly constant RU signal immediately prior to C2 injection given by the captured C4b. *B,* disruption of the C4b2 (*left*, *black curve*) and C4b2a (*right*, *red curve*) complexes by addition of 5 mM EDTA (+5 mM EDTA) and 1 M NaCl (+1 M NaCl). The beginnings of the C2 and C1s injections are indicated as "*+C2*" and "*+C1s*," respectively. The ends of the C1s, EDTA, and NaCl injections are labeled as "*stop C1s*," "*stop EDTA*," and "*stop NaCl*." *C,* injection of PMSF-inhibited C1s does not result in a two-phase dissociation curve. *D,* dissociation of C4b2 formed using either C2 WT or C2 sm in either Mg^{2+}- or Ni^{2+}-containing buffers. *E,* dissociation of C4b2a formed using either C2 WT or C2 sm in either Mg^{2+}- or Ni^{2+}-containing buffers. All SPR curves were recorded in 100 mM NaCl except for the PMSF-C1s experiment, which had 140 mM NaCl in the running buffer. *F,* isolation of C4b2a by SEC on a Superdex 200 30/100 column. *G,* SDS-PAGE analysis of C2a and C4b standards (*left*) and the peak fractions from *F* confirm the presence of only C4b and C2a in the peak from the Superdex 200 column. The bands of the C4b chains (α′, β, and γ) as well as the C2a band are indicated. The C2a band appears smeary due to its six *N*-linked glycans and overlaps slightly with the C4b β-chain. *H,* characterization of the eluate of the C4b2a elution peak by RALS and RI measurements. The correlation between RALS and RI (the *red line* of log of molecular mass estimation) suggests that the eluate is close to being monodisperse.

observations are in excellent agreement with the ability of EDTA to dissociate the AP proconvertase C3bB and its failure to promote AP convertase C3bBb dissociation (20). As for C4b2, we observed stabilizing effects on the convertase from both the two mutations and the presence of Ni^{2+}. In the presence of Mg^{2+}, the half-life of C4b2a formed with C2 sm increased by a factor of 1.8 as compared with C4b2a with C2 WT (Fig. 4*E*). The substitution of Mg^{2+} with Ni^{2+} caused a 1.6-fold increase in the half-life of C4b2a WT, whereas C4b2a with stabilizing mutations in Ni^{2+} was three times more stable

TABLE 2

Half-lives ($t_{1/2}$) in seconds for dissociation of C4b2 and C4b2a formed on the surface of an SPR sensor chip

The values were obtained by analysis of two independent experiments by the one-phase exponential decay model in GraphPad. R^2 goodness of each fit of a model to the data was >0.99.

	C4b2 at 25 °C (Fig. 4*D*, *curves*)	C4b2a at 25 °C (Fig. 4*E*, *curves*)	C4b2a at 15 °C
C2 WT, Mg^{2+} buffer	291, 246 (*black*)	1457, 1483 (*black*)	4124, 4729
C2 sm, Mg^{2+} buffer	498, 420 (*red*)	2667, 2689 (*red*)	5954, 7748
C2 WT, Ni^{2+} buffer	480, 486 (*green*)	2527, 2303 (*green*)	
C2 sm, Ni^{2+} buffer	665, 684 (*blue*)	4387, 4305 (*blue*)	

as compared with the C4b2a WT in Mg^{2+} (Fig. 4*E* and Table 2). At 25 °C, the CP C3 convertase had a $t_{½}$ of dissociation of around 72 min when C2 sm and Ni^{2+} were used to form it (Table 2).

The increased stability of C4b2a observed in the SPR studies suggested that it would be possible for the first time to conduct biophysical studies of this pivotal complex. We first investigated whether the complex could be isolated by SEC at room temperature. The resulting chromatogram suggested that in-line analysis of the C4b2a complex was feasible (Fig. 4, *F* and *G*). The homogeneity of the C4b2a-containing elution peak was assessed by the RALS and RI measurements (Fig. 4*H*). Based on the correlation between the molecular weight estimations and protein concentration, we concluded that the peak was largely monodisperse and appeared to contain molecules with a molecular mass of 241 kDa (Fig. 4*H*). This corresponds well to the molecular mass of C4b2a calculated from the protein sequence, 237 kDa, as well as to the estimated molecular mass of 258 kDa when the 10 *N*-linked and one *O*-linked glycans present on C4b2a were considered (Table 1).

SAXS Data Processing and Modeling of C4b2a—The in-line SAXS data were collected on glycosylated C4b2a subjected to SEC to maximize homogeneity of the sample and separation from C2b. We averaged the scattering data collected through the peak of C4b2a elution for every 0.058 ml of eluate and compared the R_g and the concentration-independent molecular weight estimations (25) obtained from analysis of these data blocks (Fig. 5*A*). The molecular masses obtained from the data collected in the frames 1730–1799 (10.1–10.5 ml retention volume) are in the range 242–228 kDa (Fig. 5*A*), which agrees with 241 kDa for C4b2a derived by RALS measurements (Table 1). In contrast, the data collected in the frames 1800–1869 (10.5–10.9-ml retention volume) following the scattering peak gave rise to the molecular mass estimates in the range 223–213 kDa (Fig. 5*A*). This steady decrease in molecular mass throughout the peak is likely to be caused by a constantly increasing contamination with free C4b derived from dissociation of C4b2a. Indeed, the peak of elution of free C4b overlaps with the C4b2a elution peak as judged by the SEC profiles of C4b, C4b2a, and C4b2 (Figs. 1*B* and 4*F*). However, the observation of only one peak of $I(0)$ in the in-line SAXS data suggested that there was a negligible amount of free C2a, and almost all of C2a was in complex with C4b. Additionally, prior data from hemolysis assays (15) support that the stabilization of C4b2a observed in the solid phase SPR experiment reflects the stability in solution. Assuming that the stability of the CP C3 convertase measured by SPR is similar to that in solution, we could roughly estimate how much C4b2a is left at the time of the $I(0)$ peak recording (Table 2). Approximately 35 min passed between the C4b2a complex formation and recording of the $I(0)$ peak, meaning that >75% of the total amount of C4b was in the form of C4b2a at that point based on the $t_{½}$ of 72 min estimated at 25 °C for C4b2a in the presence of Ni^{2+}. However, the temperature during the SAXS in-line experiment was around 20 °C, and our SPR data recorded at 15 °C in the presence of Mg^{2+} showed that the $t_{½}$ of C4b2a is increased by a factor of 2.5 compared with the $t_{½}$ estimated for the convertase at 25 °C (Table 2). Assuming that the same temperature effect in the presence of Ni^{2+} occurs and that at 20 °C the $t_{½}$ will be increased by a factor of 1.25 as compared with 25 °C, we estimated that >90% of C4b2a was left at the moment of recording of the $I(0)$ peak during the SAXS data collection. Therefore, we averaged the scattering data from frames 1730–1799 and used the resulting curve as the C4b2a SAXS data. The Guinier plot was linear and did not show signs of interparticle interactions, whereas the $P(r)$ function gave a D_{max} of 160 Å (Fig. 5, *B* and *C*, and Table 1). The Kratky plot (data not shown) did not indicate significant flexibility.

To conduct CORAL modeling of C4b2a, we defined three rigid bodies as follows: all the C4b domains besides the C345c domain; the C345c domain of C4b grouped with the C2a vWf domain; and the SP domain of C2a (Fig. 5*D*). The interaction between the C4 C345c and the C2a vWf domains was modeled according to the C3bBb structure (16) to keep the proper contact between the MIDAS and the C terminus of C4b. We refer to this input model as the C2a starting model. In an alternative input model, the SP domain of C2a was manually rotated away from its position in C2a (Fig. 5*E*).

The models obtained from 10 CORAL runs starting from the C2a model fitted the data with $\chi^2 = 2.20 \pm 0.53$ in scenario 1 with the C2a vWf and the SP domains coupled. The resulting models clustered very tightly (Fig. 5*F*) with the vWf domain coming close to the C4b MG7 domain and the N terminus of the C4b α' chain (the Nt-α' region), whereas the SP domain was close to the C4b MG6 domain. The biological relevance of these solutions could be evaluated by comparison with our prior model of a convertase-substrate complex based on the structure of CVF in complex with complement C5 (26). In practice, this was done by superimposing the MG1–8 domains of C4b from the C4b2a CORAL models with the MG1–8 domains of CVF in the convertase-substrate model (Fig. 5*G*). If the C4b2a models calculated by CORAL approximated an active convertase, the active site in C2a would be close to the scissile bond in the convertase-substrate model. When we in this manner evaluated the distance between the S1 pocket in C2a and the scissile bond arginine in the substrate C5, we observed only a 15 Å separation in the most favorable case (Fig. 5*H*). This was not biased by the starting model as the coupled domains (C4b

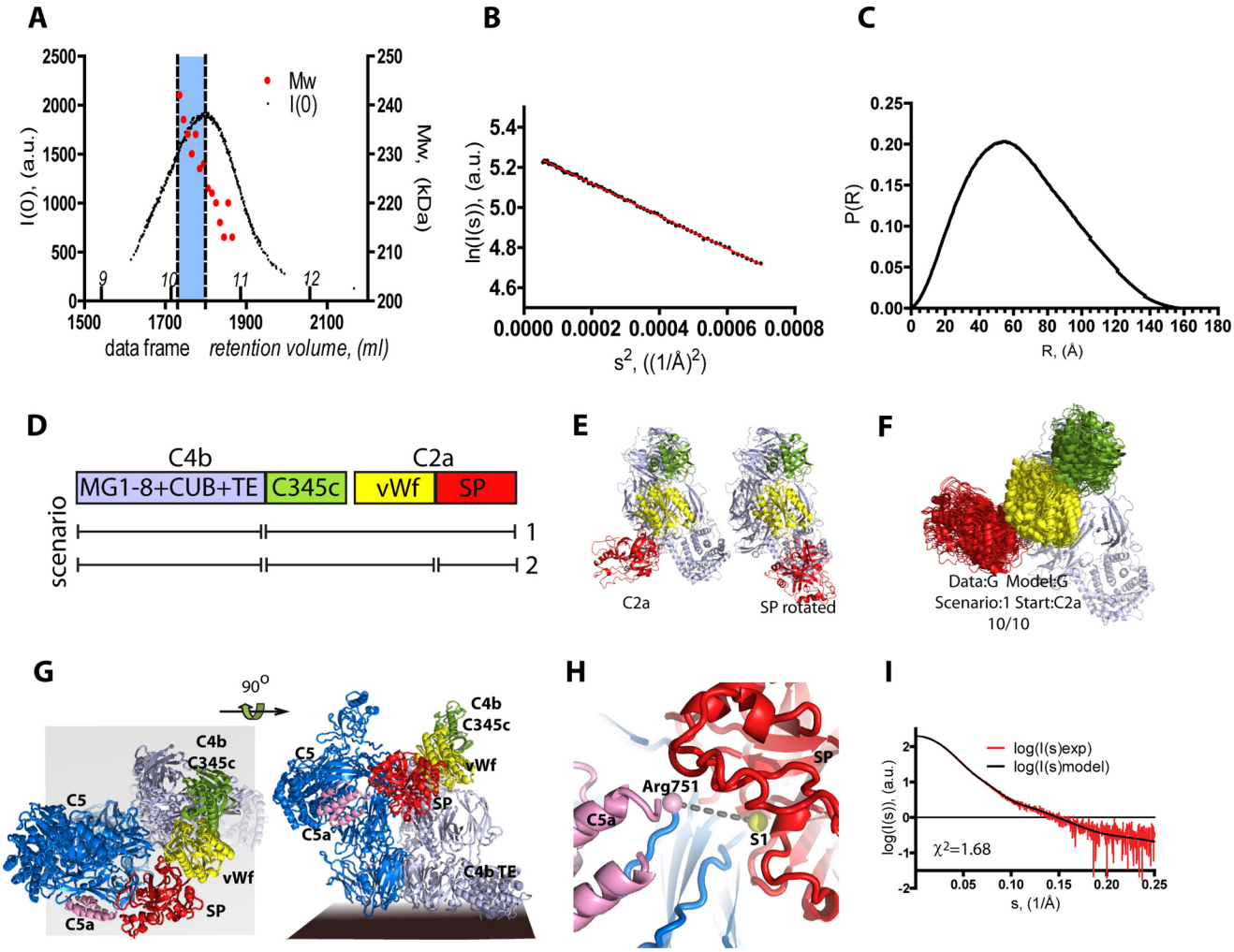

FIGURE 5. **Data collection, processing, and modeling of C4b2a.** *A,* processing of the in-line SAXS data collected during SEC with the C4b2a complex prepared as in Fig. 4*E*. The *I*(0) calculated for each recorded SAXS curve (*frame*) plotted against frame number and retention volume gave the peak of *I*(0). The data frames 1730–1799 (*blue area*) were averaged and used as the C4b2a data. *B,* Guinier plot for the data. *C, P*(*r*) function suggests a maximum inter-atomic distance of 160 Å. *D,* schematic representation of the domains in the C4b2a complex illustrating how the rigid bodies were grouped during CORAL refinements. *E,* starting model of C4b2a based on the combination of the C3bBb, C4b, and C2a crystal structures. The alternative starting model with the SP domain of C2a manually rotated is shown to the *right*. *F,* output models from scenario 1 (with the C345c, the vWf, and the SP domains grouped) cluster very tightly. *G,* superposition of one of the output models from *F* and the C5-CVF structure leads to a biologically meaningful model of the convertase-substrate complex. The substrate here is represented by the *blue* C5 molecule, in which the C5a moiety is shown in *pink*. *H,* close-up of the intermolecular interface between the C5 scissile bond region and the C2a SP domain in the model in *G*. The *dotted line* indicates the 15 Å distance between C5 Arg-751 (*pink sphere*) and the S1 pocket of C2a (*yellow sphere*). *I,* curve calculated by CRYSOL (*black*) using a representative model from *F* compared with the experimental scattering curve (*red*).

C345c, vWf, and SP) had moved significantly during refinement with an average rotation of 40° and translation of 7 Å.

Refinement under scenario 2 in which the SP domain was released from the coupled C345c-vWf domains gave three out of 10 solutions ($\chi^2 = 2.23 \pm 0.65$) with similar location of the C2a SP domain as observed in scenario 1; four of the solutions had the SP domain closer to the input model, and two had an SP domain located very far from both its starting position and the C4b MG6 domain (supplemental Fig. S1*H*). When we performed modeling under scenario 2 starting with the alternative input model where the SP domain was manually rotated away from the vWf domain (Fig. 5*E*), two out of the 10 obtained models ($\chi^2 = 2.21 \pm 0.69$) had the SP domain located near the C4b MG6 domain, suggesting that the location of the SP domain observed in scenario 1 was not biased by the starting model. However, the release of the SP domain in scenario 2 was not justified as it resulted in substantial spatial diversity between the solutions (supplemental Fig. S1*I*) and did not improve the fit to the experimental data.

One weakness of our approach was evidently that C4b2a was prone to dissociation during the in-line experiment. To exclude the possibility that the C4b2a SAXS data can be explained with a C4b model, we performed CORAL refinements using the rigid bodies only from C4b against the C4b2a data. The resulting models fitted the data poorly with an average $\chi^2 = 4.60 \pm 0.37$. To investigate how the outcome of rigid body refinement would change as a function of the input data, we prepared three alternative datasets obtained from frames 1730–1769, frames 1770–99, and frames 1800–1869, respectively (Fig. 5*A*). The two first datasets are smaller intervals of the reference data used above (frames 1730–1799), and the third larger dataset corresponds to the following 70 frames. The two smaller datasets have increased noise compared with the reference data due to data averaging of fewer frames. In the third dataset, the signal to

noise ratio is comparable with that of the reference data, but these data are expected to suffer more from C4b2a dissociation. Using scenario 1, refinement against these alternative datasets gave rise to average χ^2 in the range 2.0–2.2. For all three datasets, 8 or 9 of the 10 output models had the SP domain at the C4b MG6 domain as observed consistently with the reference dataset. This suggested that even the third alternative datasets carried enough signal from the C4b2a complex to guide the CORAL refinement.

In summary, our results showed that if properly stabilized the inherently unstable CP/LP C3 convertase may be successfully subjected to SAXS analysis. Rigid body modeling based on the resulting SAXS data gave rise to a model of the fluid phase CP/LP C3 convertase that is remarkably consistent with the model of substrate-convertase complexes obtained by combining the structures of the C5-CVF complex and the C3bBb stabilized by the protein staphylococcal complement inhibitor (SCIN) protein. In terms of biology, our results suggest that the CP C3 convertase is in a conformation not requiring major conformational changes to bind and cleave the substrate.

Discussion

The lectin and classical complement activation pathways are multistep cascades that engage several proteolytic enzymes and their large protein substrates. Structural details on how these proteins execute their function and how they interact with each other during activation are of high interest not only for the fundamental understanding of the complement system but also for therapeutic applications (27). Here we present SAXS-based structures of the three central proteins and protein complexes of these two pathways, C2, C4b2, and C4b2a, suggesting new details regarding the activation mechanism of these pathways.

Recent work on two different extracellular receptors by Savvides and co-workers (28, 29) has convincingly shown the importance of including Asn-linked glycans in SAXS rigid body modeling. The putative glycan content is 16% for C2 and 9–10% for C4b2 and C4b2a, meaning that glycans contributed significantly to their scattering curves. It was therefore important to consider how to account for these glycans during SAXS rigid body modeling. If they were included in the models, the fit of resulting solutions to the data was likely to be better as compared with models without glycans. However, our rigid body modeling made it clear that inclusion of the glycans had the cost of introducing additional degrees of freedom that could lead to overfitting of the data and potentially obscure the true protein conformation. A further complication arose for C4b2 and C4b2a because several of the Asn-linked glycans in C4b, C2, and C2a were predicted to be in proximity of the other protein within the complex assuming that C4b2 and C4b2a resemble AP complexes CVFB, C3bB, and C3bBb. As the Asn-linked glycans are unable to change conformation during CORAL refinement, they could potentially cause steric clashes in the course of the refinement that might prevent the system from reaching the global minimum. We therefore decided to also collect SAXS data from deglycosylated C2 and C4b2. For both systems, we observed that the rigid body models derived from data collected from either glycosylated proteins or enzymatically deglycosylated proteins were overall quite consistent (Figs. 2 and 3).

It is established that FB can adopt at least two conformational states, the closed and the open, which differ strongly in the arrangement of the SP domain relative to the CCP1-3 and vWf domains and in the conformation of the FB residues Arg-259–Lys-260 (19). Free FB is in the closed state in which the Arg-259 is stabilized by two salt bridges, and the SP domain is positioned to prevent effective binding of FD to FB (17, 18). Upon FB binding to C3b, the SP domain experiences a dramatic movement resulting in release of Arg-259 and exposure of the FB site for interaction with the exosite of FD (19). Our results indicated that the conformation of unbound C2 is different from either of the two FB conformations. The resolution of the SAXS data methods prevented us from deciding whether the scissile bond is protected in unbound C2. But the fact that free C2 is susceptible to C1s or MASP-1/2 cleavage *in vitro* (30, 31) suggests that the scissile bond region in free C2 is ready for cleavage unlike in unbound and CVF-bound FB.

A comparison of the C4b2 SAXS model with the crystal structures of the AP proconvertase with FB in either the closed (CVFB complex) or the open (C3bB and C3bBD complexes) conformation reveals that the overall arrangement of C4b2 corresponds to that of the CVFB complex with C2 in a conformation resembling the closed state of FB (Fig. 3, *E–H*). An equilibrium between the open and closed C4b2 conformation in analogy to C3bB in the presence of Mg^{2+} (21) is not supported by our SAXS analysis, which consistently suggested the C4b2 complex is present in only one conformation. Additionally, previous SPR binding studies on C3bB and C4b2 reported that a slow conformational change upon FB binding to C3b occurred, which can be interpreted as the transition of FB from the closed to the open state, whereas no such change happened during C4b2 formation (20, 32). Therefore, we suggest that C2 has different conformations before and after binding to C4b. Both differ from the open conformation known for FB but are cleavable by C1s and MASP-1/2. However, free and C4b-bound C2 may be cleaved at different rates as it was observed that MASP-2 cleaves C2 within C4b2 more efficiently than free C2 (31).

The cleavage mode of C2 and C4b2 proposed here is different from that for FB and C3bB. This difference may be explained by the separate settings for activation of the CP/LP and AP proconvertases. Cleavage of C2 and C4b2 is performed by the proteases C1s and MASP-1/2 associated with the pattern recognition molecules that are activated upon binding to a danger or pathogen-associated surface. Hence, the cleavage only happens when a danger is encountered and is restricted to a limited space near the activating surface (31, 33). In this manner free C2 present in the fluid phase is not activated. The case of FB and C3bB cleavage is different because FB is cleaved by the fluid phase active protease FD. FB needs to be protected from FD cleavage before the former binds to C3b. Therefore, activation of C2/C4b2 and FB/C3bB requires different modes of control. Such control is fulfilled by the proper position of the initiating complexes with proteases and C4b2 in the CP/LP or by the slow conformational change in FB and the exposure of the FD-binding site upon C3b binding in the AP. The ability of both FB and C2 to adopt two conformations appears to be a shared property, but we propose that the properties of the two zymogen confor-

mations are different for FB and C2. The AP pathway probably relies on the fluid phase FD instead of an immobilized protease as in the CP/LP to be able to cleave FB bound to the C3 tick-over product C3(H_2O) (34, 35).

We also show that activation of both the CP/LP and the AP proconvertases results in generation of structurally very similar C3 convertases. Indeed, the arrangement of the domains in our C4b2a SAXS model is almost identical to that of C3bBb in complex with the bacterial inhibitor SCIN. High structural similarity of the two complement convertases is expected due to their identical functions. In particular, both convertases cleave the same substrates, C3 and C5, that bind to the convertases presumably via the same area on C4b/C3b (26). Therefore, the arrangement of the catalytic part of the convertases, C2a and Bb, relative to the substrate binding area should be the same, which our results confirm. The 15–20 Å separation between the C2a active site of C4b2a and the scissile bond in the C5 substrate (Fig. 5*H*) obtained by combining the C4b2a rigid body model and our convertase-substrate model is very satisfying considering the following: 1) the low resolution of the SAXS data; 2) the use of a substrate-convertase model based on the C5-CVF complex; 3) the construction of a C4b2a starting model based on the C3bBb structure; and 4) the obvious possibility of local conformational differences in both substrate and convertase in the actual Michaelis complex as compared with the models presented here.

In conclusion, we have obtained solution SAXS-based structures of C2, the C3 proconvertase C4b2, and the C3 convertase C4b2a. Based on our structures of C2 and C4b2, we propose different control mechanisms for the activation of C2/C4b2 and alternative pathway proteins FB/C3bB. In particular, activation of C2/C4b2 is suggested to be controlled by positioning C4b2 near the CP/LP initiating complexes, whereas activation of FB/C3bB is restricted by the conformational change in FB, which occurs only after binding of FB to C3b. Our C4b2a model confirmed that activation of both the AP and the CP/LP proconvertases generates structurally similar C3 convertases.

Experimental Procedures

C2 Expression and Purification—Human C2 cloned into the pCEP4 vector for expression in the FreeStyle™ 293 expression system (Invitrogen) was kindly provided by Paolo Martini (Shire, Lexington, MA) (36). Site-directed mutagenesis was performed using the QuikChange Lightning site-directed mutagenesis kit (Agilent Technologies). To express the wild type or mutated protein, FreeStyle™ 293-F cells (Invitrogen) were transiently transfected using polyethyleneimine (25 kDa, Polysciences, Warrington, PA) as a transfection reagent. Conditioned medium was harvested 4–6 days post-transfection, and protease inhibitors were added to a final concentration of 10 mM benzamidine and 2 mM phenylmethylsulfonyl fluoride (PMSF). Likewise 0.09% w/v NaN_3 was added, and the pH was adjusted to pH 6.2 with acetic acid. C2 was captured from the medium on Sepharose SP beads (GE Healthcare) equilibrated in 50 mM sodium acetate (pH 6.2) and eluted with a linear gradient from 0 to 600 mM NaCl. The eluted protein was further purified by SEC on a Superdex 200 30/100 GL column (GE Healthcare) equilibrated in 20 mM HEPES-NaOH (pH 7.5), 100 mM NaCl.

Deglycosylation of C4b and C2—Human C4b was purified from outdated plasma as described previously (6). Solutions of C4b or C2 were added Tris-HCl (pH 7.0) to a final concentration of 50 mM and 10% (w/w to C4b or C2) bacterially expressed GST-tagged Endo F1, GST-peptide:*N*-glycosidase F, MBP-tagged Endo F2, and MBP-Endo F3 and incubated at 30 °C for 24 h. The enzymes were removed by affinity chromatography on GSTrap FF and MBPTrap columns (GE Healthcare). The flow-through containing deglycosylated protein was subjected to SEC on a Superdex 200 30/100 GL column (GE Healthcare) equilibrated in 20 mM HEPES-NaOH (pH 7.5), 100 mM NaCl.

C4b2 Formation—C4b and C2 were mixed at a 1:1.1 molar ratio in the presence of 2 mM $MgCl_2$ and loaded onto a Superdex 200 30/100 GL column equilibrated in 20 mM HEPES-NaOH (pH 7.5), 100 mM NaCl, 2 mM $MgCl_2$. Fractions containing the C4b2 complex were collected and used for SAXS experiments.

Site-specific Biotinylation of C4b—Nascent C4b has one free cysteine, Cys-1010 (6), which can be used to specifically label the protein (24). For the labeling reaction, purified C4 (6) was incubated with 1 mM PEO_2-maleimide-biotin (Sigma) and 0.1% w/w (to C4) of C1s (Complement Technology Inc.) in 20 mM HEPES-NaOH (pH 7.5), 100 mM NaCl. The reaction was incubated at 37 °C overnight; after that, 1% w/w (to C4) of C1 esterase inhibitor (C1INH, Complement Technology Inc.) and 5 mM L-cysteine were added to the reaction, and the mixture was incubated at 4 °C overnight. The resulting protein was dialyzed against 20 mM HEPES-NaOH (pH 7.5), 100 mM NaCl.

Surface Plasmon Resonance (SPR) Experiments with C4b2 and C4b2a—The experiments were carried out on a BIAcore T200 (GE Healthcare) with a flow rate of 30 μl/min and at 25 °C unless otherwise stated. The running buffer was as follows: 20 mM HEPES-NaOH (pH 7.5), 100 or 140 mM NaCl, 0.05% (v/v) Tween 20 supplemented with either 2 mM $MgCl_2$ or 0.5 mM $NiCl_2$. Regeneration of a sensor chip surface was obtained by injections of the running buffer free of divalent cations and supplemented with either 5 mM EDTA or 1 M NaCl. The biotinylated C4b was captured on a streptavidin sensor chip (GE Healthcare) by a 10-s injection of the protein at 30 μg/ml, aiming for ~600 RU corresponding to 600 pg/mm^2 of the immobilized protein. Absence of unspecific binding of all the tested proteins to the streptavidin sensor chip surface was confirmed by the lack of observable binding to the reference flow cell. The absence of unspecific binding of C1s (Complement Technology Inc.) to C4b2 was tested by injection of C1s with its active site blocked by PMSF. All proteins injected over the sensor chip were at a concentration of 30 μg/ml. The C2 injections were carried out until all the immobilized C4b was saturated with C2 as judged by the increasing RU reaching a plateau that corresponded well to the expected mass increase. Chased injections of C1s (60 s) were performed during the C2 dissociation phase as quickly as instrumentally possible. The data processing was done using the BIAcore evaluation software (GE Healthcare) and nonlinear regression analysis of exported data in GraphPad Prism version 5.03 to estimate half-lives based on one-phase dissociation

models for C4b2 and C4b2a complexes. The model used for analysis in GraphPad is shown in Equation 1,

$$Y = (Y_0 - \text{Plateau}) \times e^{-ikt} + \text{Plateau} \quad \text{(Eq. 1)}$$

where t is time; Y_0 is the Y value at $t = 0$; plateau is the Y at $t = \infty$, and k is the rate constant. The dissociation half-lives were calculated as $t_{½} = \ln(2)/k$. The experiments were performed in independent duplicates.

Purification of C4b2a by SEC and Analysis of C4b2a with SEC-RALS/RI/A_{280} Setup—The RALS, RI, and absorbance at 280 nm (A_{280}) data collection and analysis were performed at the EMBL Laboratory at PETRAIII, Hamburg, Germany. To prepare C4b2a, 500 μg of C4b was mixed with 230 μg of a C2 C261A/Q263K mutant in 20 mM HEPES-NaOH (pH 7.5), 100 mM NaCl, 2 mM $NiCl_2$ (final volume, 82 μl, and protein concentration, 8.9 mg/ml), and 1 μg of C1s was added to the mixture. After 5 min of incubation at room temperature, 5 μg of C1INH was added to the reaction, and the resulting mix was immediately subjected to size exclusion chromatography on a Superdex 200 10/300 GL column equilibrated in 20 mM HEPES-NaOH (pH 7.5), 100 mM NaCl, 2 mM $MgCl_2$. The SEC column was connected to a Malvern Instruments Viscotek RALS/RI/A_{280} 305 TDA detector equipped with a 670-nm laser diode to measure RALS, RI, and A_{280} of the eluate. The separation and measurements were performed at ambient temperature (20–22 °C). The molecular mass of each protein species eluting from the SEC column was estimated using concentration measurements based on RI and RALS intensities calibrated against a BSA narrow (monomeric) standard using the OmniSEC Software (Malvern Instruments).

SAXS Data Collection and Processing—The data were collected at the EMBL P12 beamline at PETRA III using a PILATUS 2M pixel detector (DECTRIS, Switzerland), an x-ray wavelength $\lambda = 1.239$ Å, and beam dimensions of 0.2 × 0.12 mm. The sample-to-detector distance was 3.1 m, covering a range of momentum transfer $0.0028 < s < 0.45$ Å^{-1} ($s = (4 \times \pi \times \sin\theta) \div \lambda$, where 2θ is the scattering angle). Data of glycosylated and deglycosylated samples of C2 and C4b2 in 20 mM HEPES-NaOH (pH 7.5), 100 mM NaCl, 2 mM $MgCl_2$ were measured in the batch setup doing 20 exposures of 0.045 s with periods of 0.05 s for each sample in a temperature-controlled cell at 10 °C with a path length of 1.5 mm. C4b2a was prepared in the same way as for SEC-RALS/RI/A_{280} measurements and loaded onto the Superdex 200 10/300 GL column equilibrated in 20 mM HEPES-NaOH (pH 7.5), 100 mM NaCl, 2 mM $MgCl_2$ at ambient temperature (~20 °C). To collect the C4b2a scattering data, 0.995-s exposures of the SEC eluate were done every second during the run. Normalization, radial averaging, buffer subtraction, and concentration correction of the C2 and C4b2 data were done at the beamline by the automated pipeline (37). Initial steps of C4b2a data processing such as radial averaging, reduction of the data frames, as well as calculation of forward scattering, $I(0)$, for each frame were done automatically as well. After the peak of $I(0)$ for C4b2a elution was detected, further processing and analysis of the data were done by manual runs of the SAXS software DATOP and DATAVER (37). R_g and $I(0)$ values were calculated using Primus QT (38) and GNOM (39). Plots were prepared with GraphPad Prism version 5.03.

SAXS Rigid Body Modeling—The rigid body refinements were done with CORAL (37) with default settings using the data range $s < 0.25$ Å^{-1}. Calculation of theoretical scattering profiles of atomic structures and their fits to the experimental data were done with CRYSOL (40). The χ^2 values calculated by CRYSOL used to assess goodness of the fits is defined as shown in Equation 2,

$$\chi^2 = \frac{1}{N} \times \left(\frac{I(s)\text{exp} - I(s)\text{model}}{\sigma} \right)^2 \quad \text{(Eq. 2)}$$

where N is a number of experimental points; $I(s)$exp is $I(s)$ of experimental data at a point; $I(s)$model is $I(s)$ of theoretical scattering at a point; and σ is the experimental error at a point. We noticed that χ^2 calculated by CRYSOL for our rigid body-derived models of C4b2a were consistently 20–25% higher than those reported directly by CORAL, which was not the case for C2 and C4b2, but for consistency we report the CRYSOL values for all three systems.

The input models for CORAL refinement of C2 were constructed by superposition of C2a (Protein Data Bank code 2ODP) and C2b (Protein Data Bank code 3ERB) onto FB in the closed conformation (Protein Data Bank code 2OK5) or in the open conformation as present in the AP proconvertase complex with FD, C3bBD (Protein Data Bank code 2XWB) (19). Input models for the proconvertase C4b2 were constructed by placing our C2 models onto the C4b crystal structure such that the C2 interface with C4b would be similar to that of FB in the CVFB complex (Protein Data Bank code 3HRZ) (18) or the C3bBD complex. Likewise, the input model for the convertase C4b2a was obtained by placing C2a relative to the C345c (C-terminal domain of complement C3, C4, and C5) domain of C4b such that it would mirror the interaction between the C3b C345c domain and Bb in the SCIN-stabilized C3bBb (Protein Data Bank code 2WIN) (16). An alternative C4b2a model was obtained from the C3bBb-like model by manual rotation of the SP domain. The missing residues in the crystal structures used to build the input models such as the C2 scissile bond containing region 226–249, the loop 707–713 in the SP domain of C2, the C termini of the α' and γ chains of C4b, and the loop 1231–1255 of C4b (6) were modeled with dummy atoms by CORAL. To add glycans *in silico* to C2, C2a, and C4b in our models, a full bi-antenna Asn-linked glycan and its attached Asn derived from Protein Data Bank code 3RY6 was superimposed onto possible rotamers of a target Asn. The rotamer superimposed glycan showing the minimal number of clashes with the protein was selected for each glycosylated Asn in C4b, C2a, and C2. The C1 atoms in all sugar residues of the glycan were renamed to Cα to impose a distance restraint (6–8 Å) between the C1 atoms in the first sugar residues and the Cα atoms of the connected asparagines and to minimize steric clashes with other rigid bodies. For refinement of C4b2 and C4b2a, a contact restraint of 10 Å preserving the C4b disulfide bridge between the Cys=1590 of the C345c domain and the Cys-876 of the MG7 (macroglobulin) domain was also introduced. Each refinement scenario was performed 10 times. Plots were prepared with GraphPad Prism 5.03.

Author Contributions—S. M. conducted all steps of protein purification, SPR data collection and analysis, SAXS data collection, data analysis, and rigid body modeling. J. K. J. guided the SPR experiments and their analysis. G. R. A. designed research. S. M., J. K. J. and G. R. A. wrote the manuscript.

Acknowledgments—We thank the beamline staff at Petra P12 for support during data collection and in particular Dr. Cy Jeffries for help with data collection and analysis of the SAXS in-line and the RALS/RI experiments. We also thank Trine Gadeberg for practical assistance. Gregers R. Andersen was supported by the LUNA Nanomedicine Center, the Lundbeck Foundation, and by the Novo-Nordisk Foundation through a Hallas-Møller Fellowship.

References

1. Ricklin, D., Hajishengallis, G., Yang, K., and Lambris, J. D. (2010) Complement: a key system for immune surveillance and homeostasis. *Nat. Immunol.* **11,** 785–797
2. Bajic, G., Degn, S. E., Thiel, S., and Andersen, G. R. (2015) Complement activation, regulation, and molecular basis for complement-related diseases. *EMBO J.* **34,** 2735–2757
3. Kojouharova, M., Reid, K., and Gadjeva, M. (2010) New insights into the molecular mechanisms of classical complement activation. *Mol. Immunol.* **47,** 2154–2160
4. Kjaer, T. R., Thiel, S., and Andersen, G. R. (2013) Toward a structure-based comprehension of the lectin pathway of complement. *Mol. Immunol.* **56,** 222–231
5. Vorup-Jensen, T., Petersen, S. V., Hansen, A. G., Poulsen, K., Schwaeble, W., Sim, R. B., Reid, K. B., Davis, S. J., Thiel, S., and Jensenius, J. C. (2000) Distinct pathways of mannan-binding lectin (MBL)- and C1-complex autoactivation revealed by reconstitution of MBL with recombinant MBL-associated serine protease-2. *J. Immunol.* **165,** 2093–2100
6. Mortensen, S., Kidmose, R. T., Petersen, S. V., Szilágyi, Á., Prohászka, Z., and Andersen, G. R. (2015) Structural basis for the function of complement component C4 within the classical and lectin pathways of complement. *J. Immunol.* **194,** 5488–5496
7. Sitomer, G., Stroud, R. M., and Mayer, M. M. (1966) Reversible adsorption of C′2 by EAC′4: role of Mg^{2+}, enumeration of competent SAC′4, two-step nature of C′2a fixation and estimation of its efficiency. *Immunochemistry* **3,** 57–69
8. Krishnan, V., Xu, Y., Macon, K., Volanakis, J. E., and Narayana, S. V. (2007) The crystal structure of C2a, the catalytic fragment of classical pathway C3 and C5 convertase of human complement. *J. Mol. Biol.* **367,** 224–233
9. Krishnan, V., Xu, Y., Macon, K., Volanakis, J. E., and Narayana, S. V. (2009) The structure of C2b, a fragment of complement component C2 produced during C3 convertase formation. *Acta Crystallogr. D Biol. Crystallogr.* **65,** 266–274
10. Miller, J. A., and Mayer, M. M. (1968) On the cleavage of C′2 by C′1a: immunological and physical comparisons of C′2ad and C′2a-i. *Proc. Soc. Exp. Biol. Med.* **129,** 127–130
11. Müller-Eberhard, H. J., Polley, M. J., and Calcott, M. A. (1967) Formation and functional significance of a molecular complex derived from the second and the fourth component of human complement. *J. Exp. Med.* **125,** 359–380
12. Nagasawa, S., and Stroud, R. M. (1977) Cleavage of C2 by C1s into the antigenically distinct fragments C2a and C2b: demonstration of binding of C2b to C4b. *Proc. Natl. Acad. Sci. U.S.A.* **74,** 2998–3001
13. Horiuchi, T., Macon, K. J., Engler, J. A., and Volanakis, J. E. (1991) Site-directed mutagenesis of the region around Cys-241 of complement component C2. Evidence for a C4b binding site. *J. Immunol.* **147,** 584–589
14. Villiers, M. B., Thielens, N. M., and Colomb, M. G. (1985) Soluble C3 proconvertase and convertase of the classical pathway of human complement. Conditions of stabilization *in vitro*. *Biochem. J.* **226,** 429–436
15. Fishelson, Z., and Müller-Eberhard, H. J. (1982) C3 convertase of human complement: enhanced formation and stability of the enzyme generated with nickel instead of magnesium. *J. Immunol.* **129,** 2603–2607
16. Rooijakkers, S. H., Wu, J., Ruyken, M., van Domselaar, R., Planken, K. L., Tzekou, A., Ricklin, D., Lambris, J. D., Janssen, B. J., van Strijp, J. A., and Gros, P. (2009) Structural and functional implications of the alternative complement pathway C3 convertase stabilized by a staphylococcal inhibitor. *Nat. Immunol.* **10,** 721–727
17. Milder, F. J., Gomes, L., Schouten, A., Janssen, B. J., Huizinga, E. G., Romijn, R. A., Hemrika, W., Roos, A., Daha, M. R., and Gros, P. (2007) Factor B structure provides insights into activation of the central protease of the complement system. *Nat. Struct. Mol. Biol.* **14,** 224–228
18. Janssen, B. J., Gomes, L., Koning, R. I., Svergun, D. I., Koster, A. J., Fritzinger, D. C., Vogel, C. W., and Gros, P. (2009) Insights into complement convertase formation based on the structure of the factor B-cobra venom factor complex. *EMBO J.* **28,** 2469–2478
19. Forneris, F., Ricklin, D., Wu, J., Tzekou, A., Wallace, R. S., Lambris, J. D., and Gros, P. (2010) Structures of C3b in complex with factors B and D give insight into complement convertase formation. *Science* **330,** 1816–1820
20. Harris, C. L., Abbott, R. J., Smith, R. A., Morgan, B. P., and Lea, S. M. (2005) Molecular dissection of interactions between components of the alternative pathway of complement and decay accelerating factor (CD55). *J. Biol. Chem.* **280,** 2569–2578
21. Torreira, E., Tortajada, A., Montes, T., Rodríguez de Córdoba, S., and Llorca, O. (2009) 3D structure of the C3bB complex provides insights into the activation and regulation of the complement alternative pathway convertase. *Proc. Natl. Acad. Sci. U.S.A.* **106,** 882–887
22. Milder, F. J., Raaijmakers, H. C., Vandeputte, M. D., Schouten, A., Huizinga, E. G., Romijn, R. A., Hemrika, W., Roos, A., Daha, M. R., and Gros, P. (2006) Structure of complement component C2A: implications for convertase formation and substrate binding. *Structure* **14,** 1587–1597
23. Roumenina, L. T., Jablonski, M., Hue, C., Blouin, J., Dimitrov, J. D., Dragon-Durey, M. A., Cayla, M., Fridman, W. H., Macher, M. A., Ribes, D., Moulonguet, L., Rostaing, L., Satchell, S. C., Mathieson, P. W., Sautes-Fridman, C., *et al.* (2009) Hyperfunctional C3 convertase leads to complement deposition on endothelial cells and contributes to atypical hemolytic uremic syndrome. *Blood* **114,** 2837–2845
24. Bernet, J., Mullick, J., Panse, Y., Parab, P. B., and Sahu, A. (2004) Kinetic analysis of the interactions between vaccinia virus complement control protein and human complement proteins C3b and C4b. *J. Virol.* **78,** 9446–9457
25. Fischer, H., de Oliveira Neto, M., Napolitano, H. B., Polikarpov, I., and Craievich, A. F. (2010) Determination of the molecular mass of proteins in solution from a single small-angle x-ray scattering measurement on a relative scale. *J. Appl. Crystallogr.* **43,** 101–109
26. Laursen, N. S., Andersen, K. R., Braren, I., Spillner, E., Sottrup-Jensen, L., and Andersen, G. R. (2011) Substrate recognition by complement convertases revealed in the C5-cobra venom factor complex. *EMBO J.* **30,** 606–616
27. Ehrnthaller, C., Ignatius, A., Gebhard, F., and Huber-Lang, M. (2011) New insights of an old defense system: structure, function, and clinical relevance of the complement system. *Mol. Med.* **17,** 317–329
28. Felix, J., Elegheert, J., Gutsche, I., Shkumatov, A. V., Wen, Y., Bracke, N., Pannecoucke, E., Vandenberghe, I., Devreese, B., Svergun, D. I., Pauwels, E., Vergauwen, B., and Savvides, S. N. (2013) Human IL-34 and CSF-1 establish structurally similar extracellular assemblies with their common hematopoietic receptor. *Structure* **21,** 528–539
29. Moharana, K., Zabeau, L., Peelman, F., Ringler, P., Stahlberg, H., Tavernier, J., and Savvides, S. N. (2014) Structural and mechanistic paradigm of leptin receptor activation revealed by complexes with wild-type and antagonist leptins. *Structure* **22,** 866–877
30. Ambrus, G., Gál, P., Kojima, M., Szilágyi, K., Balczer, J., Antal, J., Gráf, L., Laich, A., Moffatt, B. E., Schwaeble, W., Sim, R. B., and Závodszky, P. (2003) Natural substrates and inhibitors of mannan-binding lectin-associated serine protease-1 and -2: a study on recombinant catalytic fragments. *J. Immunol.* **170,** 1374–1382
31. Wallis, R., Dodds, A. W., Mitchell, D. A., Sim, R. B., Reid, K. B., and Schwaeble, W. J. (2007) Molecular interactions between MASP-2, C4, and

C2 and their activation fragments leading to complement activation via the lectin pathway. *J. Biol. Chem.* **282,** 7844–7851
32. Laich, A., and Sim, R. B. (2001) Complement C4bC2 complex formation: an investigation by surface plasmon resonance. *Biochim. Biophys. Acta* **1544,** 96–112
33. Degn, S. E., Kjaer, T. R., Kidmose, R. T., Jensen, L., Hansen, A. G., Tekin, M., Jensenius, J. C., Andersen, G. R., and Thiel, S. (2014) Complement activation by ligand-driven juxtaposition of discrete pattern recognition complexes. *Proc. Natl. Acad. Sci. U.S.A.* **111,** 13445–13450
34. Bexborn, F., Andersson, P. O., Chen, H., Nilsson, B., and Ekdahl, K. N. (2008) The tick-over theory revisited: formation and regulation of the soluble alternative complement C3 convertase (C3(H2O)Bb). *Mol. Immunol.* **45,** 2370–2379
35. Pangburn, M. K., Schreiber, R. D., and Müller-Eberhard, H. J. (1981) Formation of the initial C3 convertase of the alternative complement pathway. Acquisition of C3b-like activities by spontaneous hydrolysis of the putative thioester in native C3. *J. Exp. Med.* **154,** 856–867
36. Martini, P. G., Cook, L. C., Alderucci, S., Norton, A. W., Lundberg, D. M., Fish, S. M., Langsetmo, K., Jönsson, G., Lood, C., Gullstrand, B., Zaleski, K. J., Savioli, N., Lottherand, J., Bedard, C., Gill, J., *et al.* (2010) Recombinant human complement component C2 produced in a human cell line restores the classical complement pathway activity *in vitro*: an alternative treatment for C2 deficiency diseases. *BMC Immunol.* **11,** 43
37. Petoukhov, M. V., Franke, D., Shkumatov, A. V., Tria, G., Kikhney, A. G., Gajda, M., Gorba, C., Mertens, H. D., Konarev, P. V., and Svergun, D. I. (2012) New developments in the ATSAS program package for small-angle scattering data analysis. *J. Appl. Crystallogr.* **45,** 342–350
38. Konarev, P. V., Volkov, V. V., Sokolova, A. V., Koch, M. H., and Svergun, D. I. (2003) PRIMUS: a Windows PC-based system for small-angle scattering data analysis. *J. Appl. Crystallogr.* **36,** 1277–1282
39. Svergun, D. I. (1992) Determination of the regularization parameter in indirect-transform methods using perceptual criteria. *J. Appl. Crystallogr.* **25,** 495–503
40. Svergun, D., Barberato, C., and Koch, M. H. (1995) CRYSOL -A program to evaluate x-ray solution scattering of biological macromolecules from atomic coordinates. *J. Appl. Crystallogr.* **28,** 768–773